PUBLISHED BY THE INTERNATIONAL METEOROLOGICAL INSTITUTE IN STOCKHOLM

Tellus (2010), 62A, 319–332

TELLUS

Fine-scale model simulation of gravity waves generated by Basen nunatak in Antarctica

By TERESA VALKONEN[1]*, TIMO VIHMA[2], SHEILA KIRKWOOD[3] and MILLA M. JOHANSSON[2], [1]*Department of Physics, 00014 University of Helsinki, Finland*; [2]*Finnish Meteorological Institute, Helsinki, Finland*; [3]*Atmospheric Physics Programme, Swedish Institute of Space Physics, Kiruna, Sweden*

(Manuscript received 16 June 2009; in final form 5 March 2010)

ABSTRACT

Gravity waves over a small nunatak in Dronning Maud Land, Antarctica, were simulated applying the mesoscale model Weather Research and Forecasting (WRF). Most model experiments were made using three nested domains with 0.9 km horizontal resolution in the finest grid. The model results were validated against observations from a vertically pointing 54.5 MHz VHF radar, which provided profiles of the vertical and horizontal wind components over the nunatak. The WRF model generated gravity waves in the periods when these were observed. The modelled wave characteristics were qualitatively similar to the observed ones, although quantitative differences existed. The gravity wave had a typical vertical wave length of 3–4 km, and a maximum amplitude of 1 m s^{-1} in the vertical velocity field. The amplitude was largest at altitude of 2.0–3.5 km. The wave was strongest during nighttime, when the surface sensible heat flux was downwards. The evolution of vertical profiles of the observed rms fluctuation of vertical wind velocity and the modelled bulk Richardson number resembled each other. Gravity waves may affect the safety of aircraft landing and take-off on the lee side of the nunatak.

1. Introduction

Vertical displacement of a stably stratified flow usually leads to generation of gravity waves. Hence, gravity waves can be generated by several mechanisms, including topographic forcing, dynamic instabilities, or wave–wave interactions. Gravity waves are usually generated in the troposphere (e.g. Holton, 1992), but wave generation may also take place in the stratosphere (Yoshiki and Sato, 2000). Gravity waves are manifested as fluctuations in the velocity, pressure, and temperature fields (e.g. Rees et al., 2000). The waves transport energy away from the disturbances that generate them, and the energy is distributed horizontally and vertically up to the mesosphere and thermosphere (e.g. Holton, 1992). Gravity waves significantly influence the dynamics of the atmosphere in both small and large scales. General circulation in the mesosphere and stratosphere is strongly affected by gravity waves (Haynes, 2005). Breaking of gravity waves can cause clear air turbulence and also generate turbulence in the stable boundary layer. Orographic waves can also increase the gustiness of wind (Agustsson and Olafsson, 2004) and produce severe downslope winds (Smith, 1985; Richard et al., 1989; Mercer et al., 2008), which often pose a major challenge for operational forecasting.

In the Arctic and Antarctic, gravity waves have an important influence on the tropospheric and stratospheric circulations and chemistry. The formation of polar stratospheric clouds (PSC) is affected by gravity waves (Höpfner et al., 2006). Gravity waves generated by the mountains in the Antarctic Peninsula have several consequences in the stratosphere: forcing of the mean flow, generation of secondary inertia-gravity waves, and turbulent mixing (Plougonven et al., 2008). Model simulations by Wacker et al. (2009) suggested that gravity waves influence the mesoscale spatial distribution of precipitation in the Antarctica. Antarctic gravity waves have been studied at a number of sites: the Antarctic plateau (Kikuchi, 1988), the Antarctic Peninsula (Bacmeister et al., 1990, 1994; Alexander and Teitelbaum, 2007; Plougonven et al., 2008), and other coastal regions (King et al., 1987; Egger et al., 1993). Most of the previous studies on Antarctic gravity waves have focused on the middle-troposphere and stratosphere (Yoshiki and Sato, 2000; Fritts and Alexander, 2003; Baumgaertner and McDonald, 2007; Plougonven et al., 2008) or mesosphere and lower thermosphere (Preusse et al., 2008).

In the Antarctic coastal zone, orographic gravity waves are often excited by katabatic winds that travel down the surface slopes of the ice sheet and collide against steep cliffs along the coasts (Watanabe et al., 2006). The amplitude of such gravity

*Corresponding author.
e-mail: teresa.valkonen@helsinki.fi
DOI: 10.1111/j.1600-0870.2010.00443.x

waves is affected both by the strength of the katabatic winds (Watanabe et al., 2006) and the height of the orography (e.g. Nappo, 2002). The effects of gravity waves on mixing in the atmospheric boundary layer (ABL) have been demonstrated, e.g. by Zilitinkevich and Esau (2005). These effects are reduced in low and mid-latitudes, where stable ABL exists mainly during night-time and is separated from free atmosphere by well-mixed residual layer (e.g. Jiang and Doyle, 2008). In the Antarctic, however, stable stratification prevails in the ABL and gravity waves can penetrate from the free atmosphere to the ABL and vice versa. Hence, there are locations, such as Halley station, where ground-based instruments always detect the presence of gravity waves (Rees et al., 2000). In the ABL, wave periods range from a few minutes to about one hour and typical wavelengths extend from about 100 m to several kilometres (Rees et al., 2000). Detailed knowledge of the properties of such waves is needed for the development of parametrization schemes for use in weather forecasting and pollution dispersion models.

In this paper, we present observations and modelling of gravity waves generated by the small Basen nunatak in Dronning Maud Land, Antarctica. A nunatak is a mountain or peak not covered by ice emerging above a glacier or ice sheet. Nunataks are important in controlling the near surface wind field. Our study is based on continuous wind observations from a vertically pointing interferometric VHF radar operating at 54.5 MHz and utilization of a mesoscale atmospheric model Weather Research and Forecasting (WRF) with better than 1 km horizontal resolution. Combination of these approaches is novel. Previous observational studies on orographic gravity waves in the Antarctic have been based on satellite remote sensing (Baumgaertner and McDonald, 2007), rawinsonde data (Yoshiki and Sato, 2000), and a combination of rawinsonde, tower and microbarograph data (Egger et al., 1993; Rees et al., 2000), while modelling studies have applied more coarse grids not allowing the model to resolve small nunataks. Our objectives are to (1) validate the WRF model against the radar observations, (2) diagnose the properties of gravity waves generated by the Basen nunatak and (3) evaluate the potential effects of gravity waves generated by small nunataks.

Fig. 1. The tip of Basen nunatak pointing towards north (above). The precipice visible is the northwestern side of the nunatak, and the northeastern side behind is equally steep. The height of the precipice is 350 m. The photo below shows an Altocumulus lenticularis cloud on the lee side of the nunatak (not from the simulation periods).

2. Observations

2.1. Observation site

The observations were made on the slope of the Basen nunatak, where the Finnish and Swedish Antarctic stations Aboa and Wasa are located (73°02′38″S, 13° 24′26″W). Basen belongs to the Vestfjella Mountains in western Dronning Maud Land. Basen is situated on the lower part of the ice sheet near the grounding line, about 120 km from the ice shelf edge and 200–550 m above sea level (a.s.l.). The nunatak is approximately 4 km long and 3 km wide, with a steep northeast side (Fig. 1). The height difference between the top of the nunatak and the underlying glacier is up to approximately 350 m. Meteorological conditions at Aboa have been described by Launiainen et al. (1995) and Kärkäs (2004). The local climate on Basen is strongly affected by the topography, seen as channelling of the wind, localized convection over the snow-free surface in summer, and higher winter temperatures than on the glacier below due to a weaker inversion layer. During 1989–2001 the mean annual air temperature was −15 °C, wind speed 7.5 m s^{-1} and wind direction 30° (north–northeast).

2.2. Surface observations

At Aboa, an automatic weather station (Vaisala Milos 500) is continuously in operation. The measurement quantities include wind speed and direction at height of 5 m, 2-s gust wind speed,

Table 1. WRF simulation starting and ending times, periods of gravity wave existence and time of a strong gravity wave

No.	Simulation start	Simulation end	Wave start	Wave end	Strong wave
1	2007-12-10 00UTC	2007-12-12 18UTC	2007-12-10 01UTC	2007-12-12 18UTC	2007-12-10 06UTC
2	2007-12-29 00UTC	2007-12-31 18UTC	2007-12-30 11UTC	2007-12-31 18UTC	2007-12-31 00UTC
3	2008-01-11 00UTC	2008-01-14 18UTC	2008-01-11 11UTC	2008-01-13 06UTC	2008-01-12 12UTC

and 2-m air temperature. In addition, during the field expedition in summer 2007–2008, surface meteorological conditions were measured on the glacier below the Basen nunatak. The site (hereafter called as the 'Snow site') was located 3.4 km southwest of Aboa at 220 m a.s.l. A Metek USA-1 sonic anemometer was set up 3.5 m above the snow surface. The wind speed and air temperature were sampled at 20 Hz frequency, and the fluxes of momentum and sensible heat were calculated from the 20-Hz data using a 30-min averaging period. The results represent vertical transports including contributions of turbulence as well as inertial and gravity waves, when present. A similar sonic anemometer was set up 3.5 m above ground on the nunatak, on a rocky area on the hill top near the Aboa station, 490 m a.s.l. The air temperature and wind speed were measured on the Snow site using a 6.5-m high meteorological mast. The measurement period covered modelling periods 2 and 3 but not 1 (Table 1).

2.3. Radar measurements

MARA is an interferometric VHF radar operating at 54.5 MHz. It is located at a saddle point on the Basen nunatak, about 200 m west of the meteorological site at Aboa station. It has operated during 2 weeks in January/February 2007 and for 8 weeks in December 2007/January 2008. The measurements used here are height profiles of vertical winds determined from the Doppler shift of the returned signal, and of horizontal winds and rms velocity fluctuations determined by the full correlation technique (Briggs, 1984; Holdsworth et al., 2001; Holdsworth and Reid, 2004). This technique determines the horizontal travel speed and the decay-time of the diffraction pattern on the ground caused by radio wave scatter from the humidity and density fluctuations in the atmosphere. The only assumption required is that the temporal and spatial (horizontal) correlation functions of the fluctuations have the same shape, e.g. Gaussian. The height resolution of the measurements in the lower troposphere was 150 m in 2007 and 300 m in 2008, and in the upper troposphere, 600 m. Each profile represents an average over 30 s, with measurements repeated each 2 min. The radar antenna consisted of 48 dipole-antennas, arranged in three-square arrays, each with 16 dipoles spaced 4 m apart. This gives a beam-width of about 9° (two-way half-power full-width). Peak transmitter power was 20 kW. For further details see Kirkwood et al. (2007, 2008).

Horizontal winds are calculated from the travel time of the diffraction pattern caused by the radar echoes, as it moves across the three antenna subarrays, using the full correlation analysis (fca) technique. Figures 2 and 3 show a comparison of horizontal winds measured by the radar and by radiosondes launched from the Aboa station (Fig. 2) or from the Snow site on the glacier (Fig. 3). There are gaps in the height coverage of the radar winds when the echo signal strength is low, which often happens for the upper troposphere, and for heights more than 1000–2000 m above the tropopause. There is generally good agreement between the radar and sonde winds, except below 2000 m, where

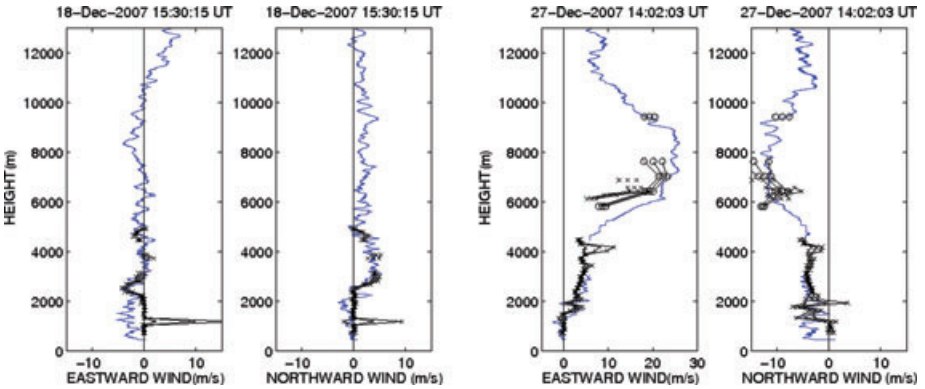

Fig. 2. Comparison of winds from MARA (black) and from GPS radiosondes (blue) launched from Aboa station on 18 and 27 December, 2007. Results are shown from two different radar operating modes, one for upper troposphere with 600 m (circles) height resolution and one primarily for lower troposphere with 150 m height resolution. For each mode there are three profiles, the mean profile, and the mean plus or minus the standard error of the mean, derived by averaging over the period from 2 h before to 2 h after the radiosonde launch. Gaps in the height coverage correspond to signal-to-noise ratio less than one.

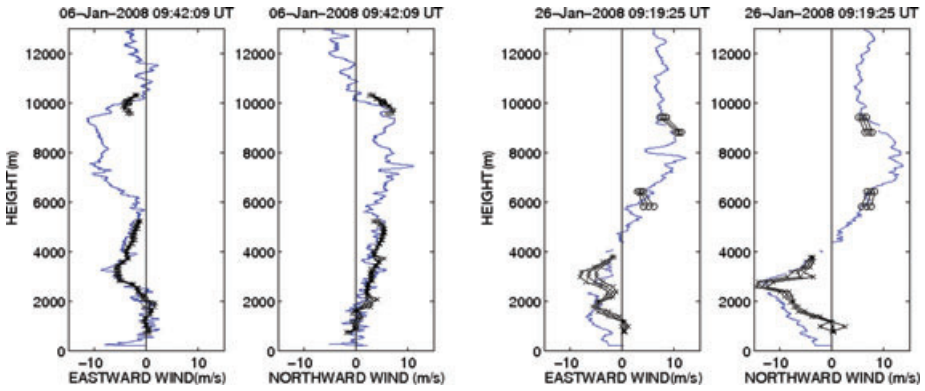

Fig. 3. As Fig. 2 but for GPS sondes launched from the snow site on 06 and 26 January 2008. Crosses are for a radar mode with 300 m height resolution.

interference from ground reflections gives problems for the radar wind analysis.

Vertical wind estimates from the radar cannot be validated by radiosondes but their derivation is direct from the Doppler shift of the returned signal. They have a much lower intrinsic uncertainty than the horizontal winds.

The rms velocity fluctuations are calculated from the decay time of the diffraction pattern caused by the radar echoes, as it moves across the antenna array.

$$V_{\mathrm{RMS}} = \lambda \frac{\sqrt{2 \ln 2}}{4\pi\tau}, \tag{1}$$

where λ is the radar wavelength, and τ the intrinsic half-life time of the diffraction pattern. This represents the standard deviation of vertical velocities of scatterers within the scattering volume, over the time of each measurement (30 s), provided that this vertical motion is the dominating factor determining the correlation time of the diffraction pattern. In the case that the volume is filled with turbulent eddies, this can be expected to be the case. As discussed in Holdsworth et al. (2001), the fca technique together with an interferometric antenna array such as that used by MARA, gives a direct estimate of V_{rms}. There is no need for the kind of beam-width/wind-speed corrections which must be applied in the case of non-interferometric Doppler-beam-swinging radars which estimate V_{rms} from the spectral width of the echoes. The MARA data indicated strongest signals of gravity waves on 10th and 31st of December 2007 and 12th of January 2008.

3. Model experiments

3.1. Three-dimensional numerical weather prediction model

The Weather Research and Forecasting (WRF, http://wrf-model.org) is a modelling system developed in the USA by a collaborative partnership during past few years. The Advanced Research WRF (ARW) is designed to be a flexible, state-of-the-art atmospheric simulation system that can be used both for research and operational purposes (Skamarock et al., 2007). The WRF model is a fully compressible non-hydrostatic model, which uses the Runge–Kutta second- and third-order time integration schemes, and second- to sixth-order advection schemes. The vertical coordinate of the model is a traditional terrain-influenced σ coordinate. The model variables are horizontally staggered in an Arakawa C-grid. The WRF model has multiple physics packages available for parametrization of the surface, atmospheric boundary layer, radiation and cloud physics.

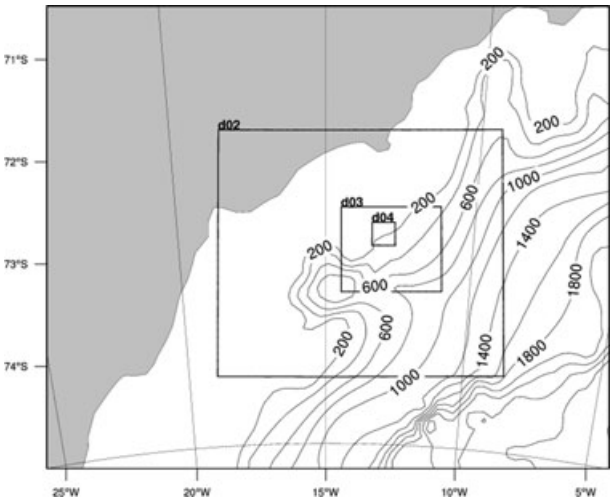

Fig. 4. Nested WRF model Domains 1-4. The Basen nunatak is situated in the middle of the fourth domain. Domains 3 and 4 are shown in more detail in Fig. 5. Grey colour indicates sea area whereas white the glacier. The topography is shown on black contours in 200 m interval.

3.2. Domains and boundary data

The model system in this study consists of polar stereographic domains at the horizontal resolution of 8.1, 2.7, 0.9 and 0.3 km (Fig. 4). Domains 3 and 4 are shown in more detail in Fig. 5. After analysing the wind observations, three periods were

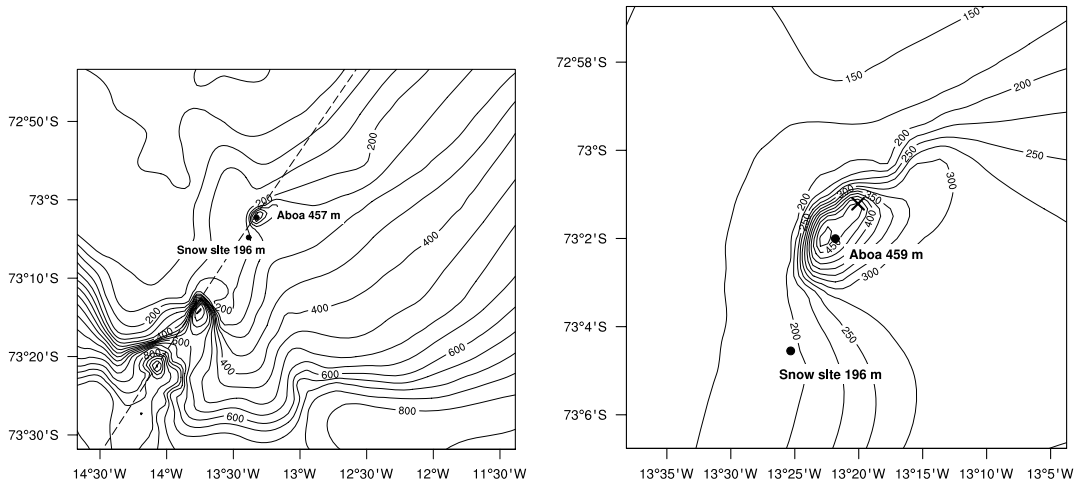

Fig. 5. WRF model Domains 3 (left-hand panel) and 4 (right-hand panel). Locations and heights of Aboa and the Snow site are marked with filled circles. The dashed line in Domain 3 denotes the cross-section of model results shown in Figs. 10 and 11. The cross in Domain 4 marks the location of the northern tip of the nunatak, shown in Fig. 1.

chosen to be simulated in austral summer 2007–2008 (Table 1). All the periods were simulated with Domains 1–3 while the last period was also simulated with all four domains. This was done to see if we can achieve any benefit from the 0.3 km resolution. In the vertical, a total of 57 levels were used. The lowest model level was approximately at 26 m above surface of the nunatak. The model top was set at 50 hPa.

The model was initialized by the European Centre for Medium-Range Weather Forecasts (ECMWF) operational analyses, which has a horizontal resolution of 0.2°. The 6-hourly analyses were used to provide lateral boundary conditions during the simulations. At the lower boundary of the model, the terrain elevation is specified by the data from the Radarsat Antarctic Mapping Project Digital Elevation Model Version 2, resolution of 1 km (Liu et al., 2001). Elevations for points in this data set are measured in metres above the OSU91A geoid. The OSU91A geoid is a complex surface representing the mean sea level. The land use is specified by 25-category data of the U.S. Geological Survey.

3.3. Physical parametrizations

In this study cloud microphysics is parametrized applying the Thompson et al. (2004) scheme which has ice, snow and graupel processes suitable for high-resolution simulations. The scheme includes six classes of moisture species plus number concentration for ice as prognostic variables.

Longwave radiation is treated with the Rapid Radiative Transfer Model scheme (RRTM) based on Mlawer et al. (1997). It is an accurate scheme using look-up tables for efficiency. The RRTM accounts for multiple bands, trace gases, and microphysics species. Shortwave radiation is parametrized with Dudhia scheme (Dudhia, 1989). The scheme has simple downward integration allowing efficiently for clouds and clear-sky absorption and scattering.

The surface layer is parametrized with Skamarock et al. (2007) scheme. The scheme calculates friction velocities and exchange coefficients that enable the calculation of surface heat and moisture fluxes by the land-surface model and surface stress in the atmospheric boundary layer scheme. The land surface is treated with 5-layer thermal diffusion land surface model (Skamarock et al., 2007). This simple model is based on the 5-layer soil temperature model of the fifth-generation National Center for Atmospheric Research NCAR/Penn State Mesoscale Model (MM5). Layers are 1, 2, 4, 8 and 16 cm thick and the temperature is constant below the lower most layer.

The atmospheric boundary layer is parametrized with the Yonsei University (YSU) scheme described by Hong et al. (2006). The scheme is responsible for vertical subgrid-scale fluxes due to eddy transports in the whole atmospheric column. It employs a so-called counter-gradient flux for heat and moisture in unstable conditions and has an explicit treatment of the entrainment layer at the boundary layer top. The latter is based on results from large-eddy simulations (Noh et al., 2003). In the scheme, the ABL top corresponds to the maximum entrainment layer, and is defined using a critical bulk Richardson number (Ri) of zero. Ri was calculated on the basis of the modelled wind speed and potential temperature as follows:

$$Ri = \frac{g}{0.5(\theta_i + \theta_{i+1})} \frac{\theta_{i+1} - \theta_i}{(u_{i+1} - u_i)^2} (z_{i+1} - z_i), \tag{2}$$

where θ is the potential temperature, u is the horizontal wind speed, g is the acceleration due to gravity, z is height and index i refers to the model level ($i = 1$ for the lowest level). Ri is accordingly calculated for heights $(z_i + z_{i+1})/2$. The WRF

method to calculate the ABL top is, however, not good for a stable boundary layer that is not capped by a residual layer.

4. Results

4.1. Comparison of observations and model results

Time series of the near-surface (10 m in WRF, 3.3 m in the observations) wind speed, friction velocity, 2-m air temperature, and sensible heat flux are shown in Fig. 6. WRF well reproduced the timing of the variability, but overestimated the diurnal cycle of air temperature. Our radiation measurements indicated that the albedo at the snow-covered site ranged from 0.8 to 0.9. The WRF model used, however, a summertime albedo of 0.55 for snow and ice. This is a clear reason for the overestimation of the diurnal temperature cycle over the snow-covered glacier. At the rocky site next to the Aboa station the true albedo was close to 0.1., but the WRF model considered all the nunatak as snow-covered, and therefore applied the albedo of 0.55 also over the rocky Aboa site. The diurnal temperature cycle was, however, overestimated also over the rocky site. This was because the air temperature did not immediately respond to the local fluxes over the small rocky area, but was strongly affected by horizontal advection from the snow-covered areas, where the diurnal cycle was overestimated.

The friction velocity was very well simulated but the wind speed was simultaneously underestimated. This was due to a too high momentum roughness length z_0 of 0.05 m applied in WRF over snow and ice. Field observations indicate that z_0 for a snow-covered glacier is typically 10^{-4} to 10^{-3} m (King and Turner, 1997). WRF reproduced the spatial differences between the Snow site and Aboa. The Aboa weather station data also allowed calculation of the wind gust factor, here defined as the ratio of the gust wind and the hourly mean wind (using hourly values instead of 10 min values yields somewhat higher gust factors). During the simulation periods the gust factors ranged from 1.1 to 2.6, with the mean value of 1.3. The gust factor and mean wind speed had a correlation coefficient of −0.68. When

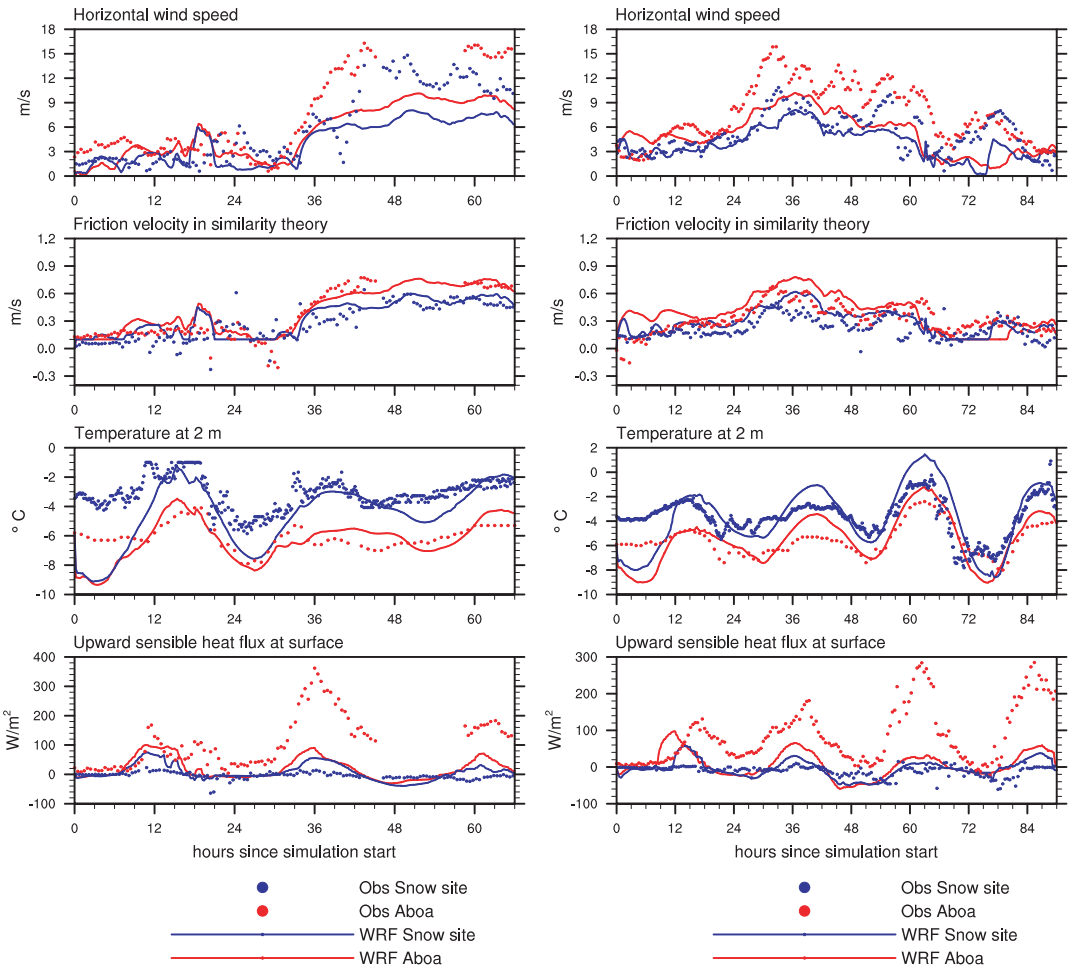

Fig. 6. Time series of wind speed, friction velocity, air temperature, and sensible heat flux at the Aboa station and the Snow site during the second (left-hand panel) and third (right-hand panel) simulation period.

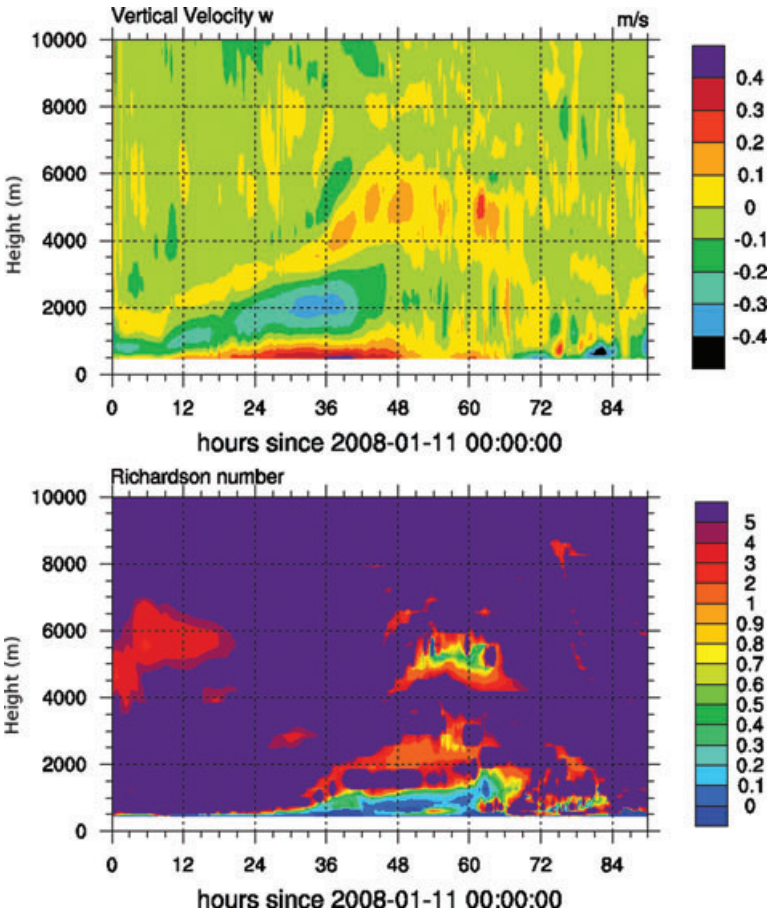

Fig. 7. Time-height diagrams of the modelled vertical velocity (top panel) and bulk Richardson number (bottom panel) at Basen nunatak from the third simulation period.

the gravity wave was most visible (Table 1), the gust factor was low, on average 1.1. In general, gravity waves tend to increase gustiness (Agustsson and Olafsson, 2004). On the other hand, they occur during stably stratified conditions, and strong stability itself reduces the gust factor (Brasseur, 2001). It seems that the latter effect dominated in the cases observed. Further, the gust factor was measured near the surface, while the gravity wave was probably most pronounced at higher elevations.

From the point of view of gravity waves, the most essential model validation is that based on the vertical profile data from MARA. Figure 7 shows time-height diagrams at Basen nunatak for the third simulation period. The upper panel of Fig. 7 on the vertical velocity suggests that the gravity wave is strongest on 12 January approximately at 12 UTC, i.e. 36 h after the start of the simulation. Later, approximately from 36 to 66 h after the simulation start, Ri decreases, the minimum being below 0.2 (lower panel in Fig. 7). The change to dynamically unstable conditions is related to weakening of the wave. Figure 8 shows analogous results from MARA measurements: the vertical wind velocity and the rms velocity fluctuation (see eq. 1), the latter characterizing turbulence.

The shape of the vertical wind patterns in Figs. 7 and 8 is qualitatively similar, demonstrating a good agreement between MARA and WRF results. The main differences are related to the timing of the maximum downward winds at the altitude of approximately 2 km: in WRF these occur 30–39 h after the simulation start, while MARA detected them 1–35 h later. MARA also detected stronger downward winds around 6 km altitude. The MARA and WRF results for the altitudes and time periods of occurrence of strongest turbulence also agree qualitatively: lowest Ri and highest rms velocity fluctuation occur below 2 km altitude and mostly in the middle of the simulation period. During the first 15–20 h, WRF yields a pattern of lower Ri and MARA a pattern of higher velocity fluctuation, but in the MARA results the altitude is about 1 km higher. During simulation periods 1 and 2 the agreement between MARA and WRF was qualitatively similar to that during period 3.

Figure 9 shows MARA- and WRF-based profiles of the vertical wind component in the three cases simulated. The mean bias and root-mean-square error (RMSE) of the vertical profiles are shown in Table 2. The vertical wind velocity is negatively biased in all model simulations, but the smallest bias and RMSE are found in the third WRF simulation with a horizontal resolution of 0.3 km. These results together suggest that the smoother topography in the model compared to reality results in a weaker gravity wave.

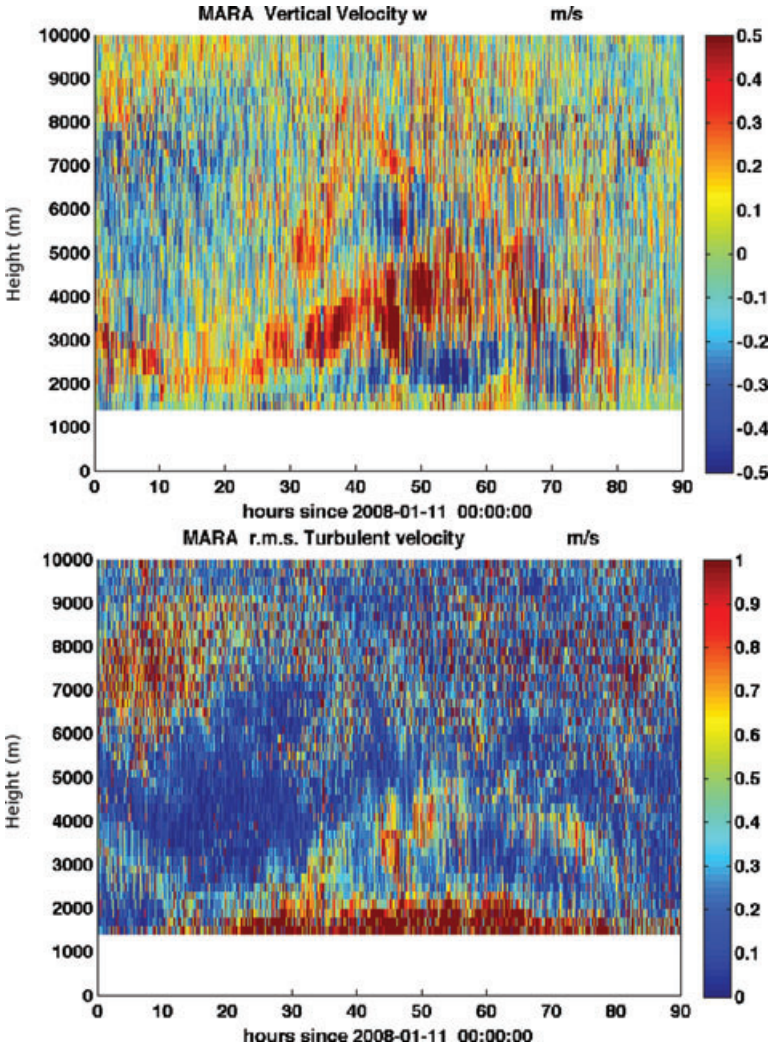

Fig. 8. Time-height diagrams of vertical velocity (top panel) and rms velocity spread (bottom panel) from MARA observations during the third simulation period.

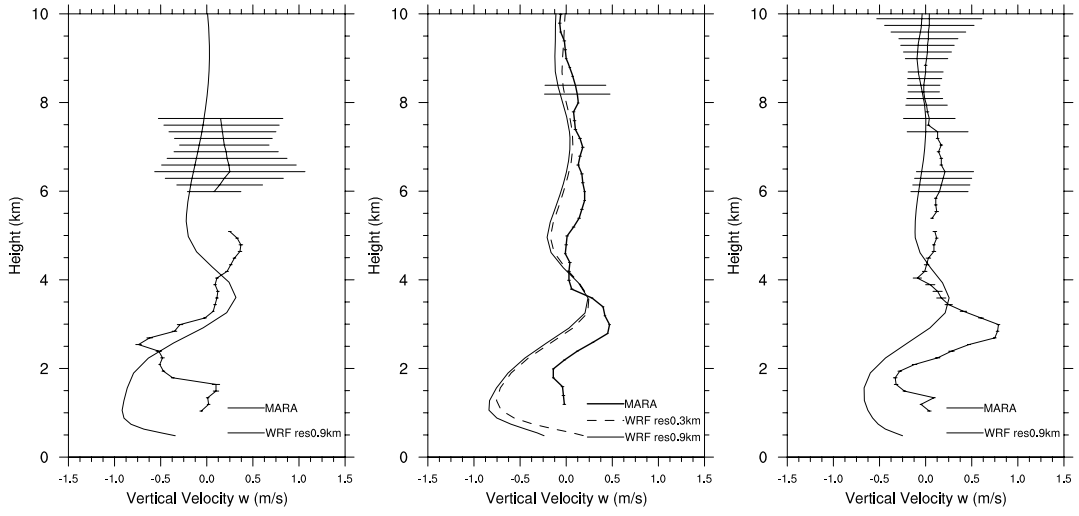

Fig. 9. Profiles of vertical wind velocity at Basen nunatak at 2007-12-10 06 UTC (left-hand panel), 2007-12-31 00UTC (middle panel) and 2008-01-12 12UTC (right-hand panel) from WRF simulations and MARA measurements.

Table 2. Model errors for the vertical wind velocities at the time of the strongest gravity wave in the three cases simulated

No.	Model	Bias ($m\,s^{-1}$)	RMSE ($m\,s^{-1}$)
1	WRF res 0.9 km	−0.24	0.43
2	WRF res 0.9 km	−0.21	0.32
3	WRF res 0.9 km	−0.24	0.33
	WRF res 0.3 km	−0.20	0.29

The peak values of vertical wind velocities decreased with height because the maxima and minima were moved downstream of the nunatak with the prevailing wind (Fig. 9). Also, the horizontal wind was stronger at higher altitudes, which caused damping of the wave. The radar observations were made directly above the nunatak and therefore we have to compare the model data from the same vertical axis. The observed maxima of the vertical wind speed were located at slightly lower altitude than modelled ones in simulations 1 and 2. The model produced the largest magnitude of vertical velocities close to the ground. The radar measurements were, however, reliable only from 2 km upwards. Above that level, the observed peak values of vertical velocity were higher than modelled ones, especially around 3 km above sea level.

As a summary, applying 0.9 km horizontal resolution, WRF can generate gravity waves in the periods when these were observed over the Basen nunatak. The modelled wave was qualitatively similar to the observed one, although quantitative differences existed.

4.2. *Modelled wave characteristics*

The rest of the results presented are only based on WRF. Figure 10 present cross-sections of the vertical wind velocity in the three cases. The location of the cross-section is marked in Fig. 5. Basen is located at grid point 70 on the horizontal axis and the flow comes from the right-hand side of the figure. Common features between the three cases are that there are no gravity waves upwind of Basen, but strong waves are generated both by Basen and the higher nunataks downwind of it. Due to the 20 km fetch over a flat glacier, the gravity wave generated by Basen is distinguishable from the waves further downwind, while at grid points 1–50 the waves generated by neighbouring nunataks interact non-linearly with each other. In case 1 the wave generated by Basen penetrates through the troposphere, while in cases 2 and 3 the damping with height is stronger. In other respects, the locations and shape of the regions of upward and downward velocity are very similar between the three cases simulated.

Wave characteristics were calculated from the cross-sections every hour when the gravity wave was visible. Two lowest minima and two lowest maxima of the vertical wind velocity were

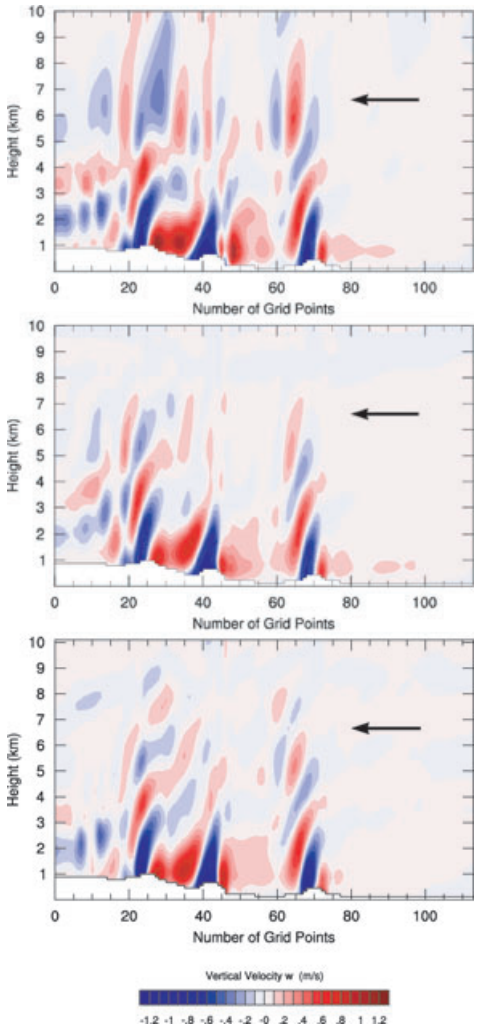

Fig. 10. Cross-section of modelled vertical wind velocity for 2007-12-10 06 UTC (top panel), 2007-12-31 00UTC (middle panel) and 2008-01-12 12UTC (bottom panel). Basen nunatak is located at grid point 70 on the horizontal axis. The arrows indicate the flow direction.

taken into account when calculating the amplitude from the WRF model data. The amplitude of the wave was defined as the difference between the adjacent minima and maxima divided by two, and the values were averaged for each hour.

We further calculated the Scorer parameter (l^2) and Froude number (Fr). The Scorer parameter (Scorer, 1949) was calculated as follows:

$$l^2 = \frac{N^2}{u^2} - \frac{\frac{\partial^2 u}{\partial z^2}}{u}, \tag{3}$$

where N is Brunt–Väisälä frequency defined as $N = \sqrt{\frac{g}{\theta}\frac{d\theta}{dz}}$. Both N and u were calculated on the basis of the model output fields. The second derivative was approximated by a finite difference in the model grid. Following Baines (1995), we calculated

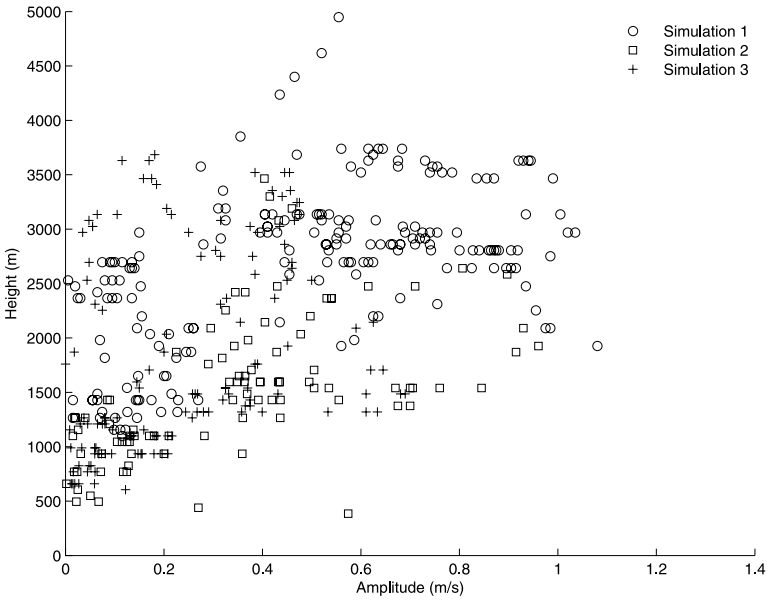

Fig. 11. Modelled amplitude of vertical wind velocity as a function of height in three simulations.

the Froude number as

$$Fr = \frac{u}{NL}, \tag{4}$$

where L is the width of the nunatak in the direction of the flow.

The modelled wave amplitude of the vertical velocity field showed a growing trend with height (Fig. 11). Only two maxima and minima closest to the surface were, however, considered. Typically above that the amplitude was weaker. The strongest amplitude was modelled at 2–3.5 km height, where it reached up to 1 $\mathrm{m\,s^{-1}}$. At the horizontal location of the gravity wave generated by Basen, in cases 1 and 3, l^2 reached its maximum at the height of 3.7–4.0 km, while in case 2 the maximum was reached at the height of 4.9 km. The cross-section of l^2 in case 1 differs, however, strikingly from that in cases 2 and 3: in case 1 l^2 changes very little in the layer from 6–7 to 9.5 km (Fig. 12). When l^2 is nearly constant in height, conditions favour vertically propagating gravity waves, whereas trapped lee waves can be expected when l^2 strongly decreases with height. Hence, in case 1 the nearly constant l^2 in the layer from 6–7 to 9.5 km allows the gravity wave propagate much higher than in cases 2 and 3 (compare Figs. 10 and 12). It is noteworthy that case 1 also includes a downstream region (grid points smaller than 30 in Fig. 12) where l^2 strongly decreases with height from 4 to 6 km. The very strong wave generated by the nunatak at grid points 20–30 indeed strongly attenuates in this region, and does not propagate as high as the wave generated by the nunatak at grid points 40–45.

When defined as in (4), *Fr* represents the ratio of the natural wavelength of vertical oscillations in the atmosphere to the wavelength of the mountain (e.g. Barry, 2008). In all three cases, *Fr* just above Basen was close to unity (from 0.7 to 1.2), which favours the generation of strong mountain waves. In cases 1 and 2 the Froude number is, however, everywhere less than 1, indicating a sub-critical flow, where a wave can penetrate upstream. In case 3, *Fr* slightly exceeds 1 in the lowest hundreds of metres above Basen and the next nunatak downstream. This is in agreement with the fact that some upward vertical velocity is detected already over the flat glacier upstream of Basen in cases 1 and 2 (top and middle panels in Fig. 10) but not in case 3.

The evolution of the modelled sensible heat fluxes over the Basen nunatak during the three simulation periods is shown in the top panel of Fig. 13. The boundary layer height is closely related to the surface sensible heat flux and it has a diurnal cycle as well. WRF seems, however, to exaggerate the diurnal cycle of the ABL height. Anyhow, the 350-m-high nunatak can generate gravity waves even in the afternoon, because the vertical displacement of the air takes place not only in the neutral boundary layer but also in the stable layer above it. The wave has, however, largest amplitude of the vertical velocity at nighttime when the sensible heat flux is negative and the boundary layer is shallowest. The heat flux correlates negatively with the wave amplitude of the vertical velocity, the correlation coefficient being −0.39.

5. Discussion

Compared to previous studies on gravity waves in the Antarctic, the main advance by the present study is the combined use of continuous observations of the vertical profile of horizontal and vertical wind components and the application of a high-resolution mesoscale model.

The validation of the WRF model indicated that applying 0.9 km horizontal resolution, WRF was able to generate gravity waves in the periods when these were observed by the MARA radar above the Basen nunatak. The modelled wave

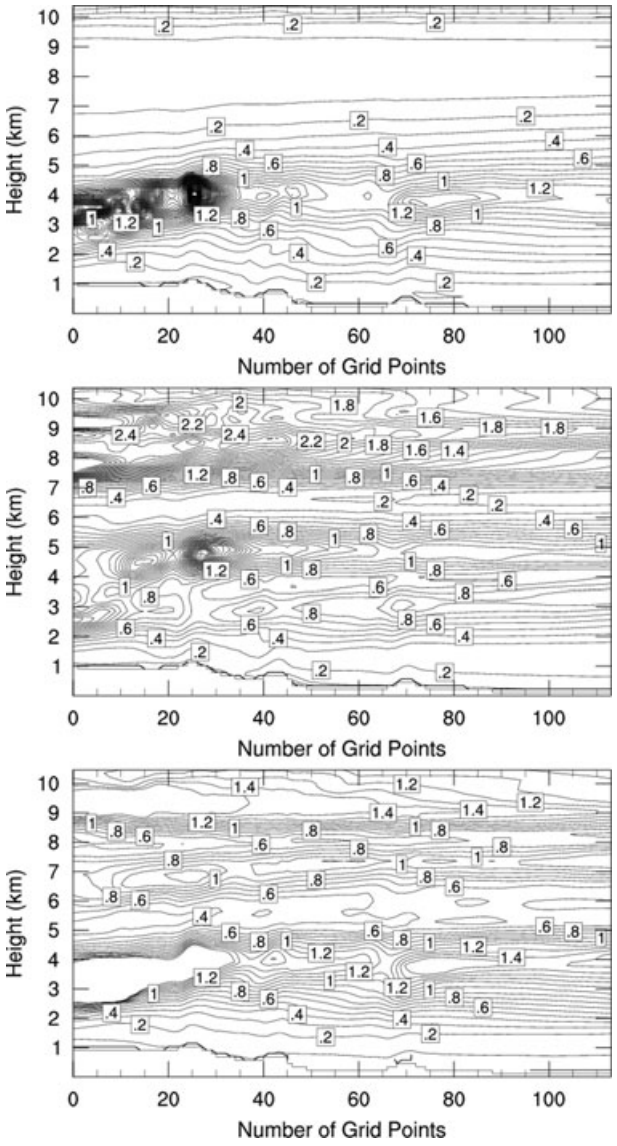

Fig. 12. Cross-section of modelled Scorer parameter $\times 10^{-6}$ m^{-2} for 2007-12-10 06 UTC (top panel), 2007-12-31 00UTC (middle panel) and 2008-01-12 12UTC (bottom panel). Contours are plotted up to 10×10^{-6} m^{-2} on 0.1×10^{-6} m^{-2} interval. Basen nunatak is located at grid point 70 on the horizontal axis.

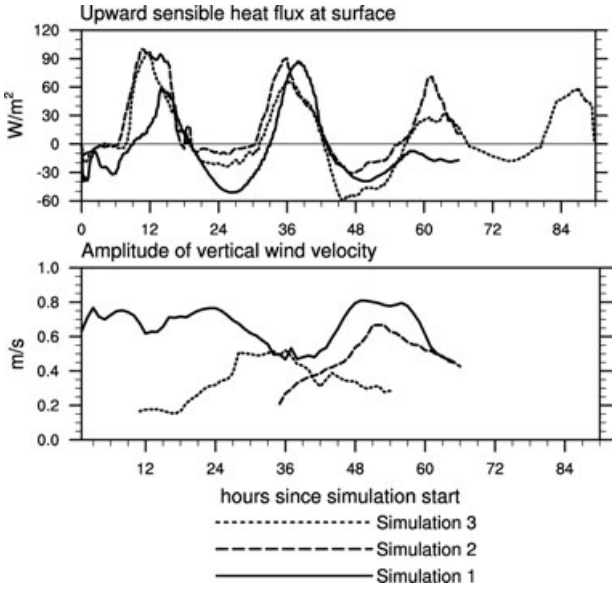

Fig. 13. Evolution of the modelled surface sensible heat flux, and amplitude of vertical wind velocity at Basen from three WRF simulations.

characteristics were qualitatively similar to the observed ones, although the observed and modelled vertical velocity fields were not exactly equal. Increasing the horizontal resolution from 0.9 to 0.3 km only slightly improved the results.

The gravity wave over Basen had a maximum amplitude of approximately 1 m s^{-1} in the vertical velocity field. The amplitude was largest at the altitude of 2.0–3.5 km. The Froude number favoured generation of strong gravity waves. In agreement with previous studies (Whiteway and Duck, 1996), the wave was strongest during strong winds. The crests downwind of the ridge favoured the formation of a wave cloud, which was indeed observed over the nunatak (Fig. 1). During the three study periods, the gravity wave over Basen was very stationary at the lower parts. At higher altitudes the wave was more affected by the prevailing wind conditions and the vertical damping varied between the cases. The damping was basically in agreement with the distribution of the Scorer parameter, which explained why the wave generated by Basen propagated much higher in case 1 than in cases 2 and 3. It also explained why the stronger wave generated further downstream in case 1 rapidly attenuated at the heights of 4–6 km. The wave attenuation and the vertical gradients in the Scorer parameter did not, however, exactly match in all periods and parts of the study region. As the results for the gravity waves and Scorer parameter were based on the same model simulations, the unexplained features suggest an influence of three-dimensional or non-linear wave properties that cannot be presented by the Scorer parameter. The topography of the study region may indeed generate three-dimensional features.

The Basen nunatak has a maximum height of 350 m only but is still capable of generating strong gravity waves. On the basis of rawinsonde sounding data from the Antarctic stations Syowa and Casey, Yoshiki and Sato (2000) concluded that topographically generated gravity waves in the Antarctic usually do not reach altitudes higher than 5 km, where the easterly wind in the lower troposphere climatologically decreases to zero. They accordingly concluded that stratospheric gravity waves in the Antarctic have their source in the stratosphere, with the polar night jet as a potential candidate. In our three study periods, the gravity waves typically extended up to the heights of 6–7 km, roughly in agreement with Yoshiki and Sato (2000), but

in Period 1 a weaker wave was still present well above 10 km altitude. This demonstrates that mountain waves generated by a small nunatak can reach the lower stratosphere, at least in cases when there is not too much shear in the zonal wind.

During the strongest wave periods the gust factor was only 1.1. On the basis of observations in Iceland, Agustsson and Olafsson (2004) found out that measurement sites downwind of mountains are associated with high gust factors, and further suggested that gravity waves increase the gust factor. On the other hand, gravity waves occur during stably stratified conditions, and strong stability itself reduces the gust factor (Brasseur, 2001), which seems to have dominated during the study period at Aboa. The negative correlation we observed between the mean wind speed and gust factor is in agreement with Agustsson and Olafsson (2004). However, Agustsson and Olafsson (2004) studied highly non-linear waves whereas the waves in our study were nearly linear or only weakly non-linear.

Although the gravity waves addressed in this study were generated by the local topography, this is not always the case for gravity waves observed in the Antarctic ABL. Egger et al. (1993) described two gravity wave events detected at the Neumayer Station 400 km northeast of Basen. In the first case, the wave was probably generated by motion of a coastal frontal zone separating air masses, while in the second case topographic influence may have been important. As Neumayer Station is located on a flat ice shelf, the topographic wave must have been trapped to reach the surface observation site. Our results for Basen did not show signs of wave trapping. Rees et al. (2000) compiled a climatology of gravity waves, in the period range 1-20 min, propagating in the stably stratified ABL overlying the ice shelf at Halley. They studied wave properties in conjunction with the mean wind and temperature profiles in the ABL, and found that most of the wave activity did not originate locally, but from shear layers aloft, or, more commonly, from the katabatic flow regime where the ice shelf joins the Antarctic continent. At Halley, Rees et al. (2000) mostly observed propagating internal gravity waves, while the gravity waves at Basen were standing ones. The difference is probably related to the fact that Halley is located on a very homogeneous ice shelf, with a 40 km distance to the region of irregular terrain. Hence, there were no locally generated standing waves.

According to our WRF results the gravity wave amplitude correlated negatively with the surface sensible heat flux, which is strongly related to the ABL height. This confirms the results of previous idealized model experiments not directly validated against observations. Olafsson and Bougeault (1997) concluded that the ABL tends to weaken mountain waves, reduce wave drag, and delay the onset of wave breaking. Jiang and Doyle (2008) and Jiang et al. (2008) found out that the wave drag strongly depends on the ABL height and stability. A convective ABL significantly weakens mountain waves. Also the idealized simulations of Peng and Thompson (2003) demonstrated that in general the ABL decreases the wave amplitude.

Our study period was in austral summer, when both atmospheric pressure gradient and ABL stratification in the Dronning Maud Land are weakest (King and Turner, 1997). Hence, we can expect even stronger gravity waves in the region in other seasons. From the point of view of precipitation, gravity waves generated in autumn are probably the most important ones. Autumn is the season with peak precipitation in the Antarctic coastal zone (Tietäväinen and Vihma, 2008) and gravity waves may affect its spatial distribution (Wacker et al., 2009). The Basen nunatak is probably climatologically important for the regional gravity wave field, as the prevailing wind direction is from 30°, i.e., towards the steep side of the nunatak. Downwind of Basen, stronger gravity waves are generated by the higher nunataks. The gravity wave field over Basen is, however, seldom affected by them, as winds from south–southwest are rare (Kärkäs, 2004). In addition to the general importance of gravity waves (Section 1), gravity waves over Basen probably decrease aviation safety, as the airfield serving Aboa and Wasa stations locates on the lee side of the nunatak. This study demonstrates that by operational high-resolution modelling the dangerous wave events could be forecasted. The gravity waves over Basen may also cause strong variations in aerosol and ozone concentrations (Virkkula et al., 2009).

6. Acknowledgments

This study was supported by the Academy of Finland (contracts 128799, and 128533). Knut and Alice Wallenbergs foundation and the Swedish Research Council have provided financial support for the MARA radar and for the radiosondes. The logistics groups of FINNARP and of SWEDARP, and I. Wolf of the Swedish Institute of Space Physics, are acknowledged for support during the field expedition.

References

Agustsson, H. and Olafsson, H. 2004. Mean gust factors in complex terrain. *Meteorologische Zeitschrift* **13**, 149–155.

Alexander, M. J. and Teitelbaum, H. 2007. Observation and analysis of a large amplitude mountain wave event over the Antarctic peninsula. *J. Geophys. Res.* **112**(D21103). doi:10.1029/2006JD008368.

Bacmeister, J. T., Newman, P. A., Gary, B. L. and Chan, K. R. 1994. An algorithm for forecasting mountain wave-related turbulence in the stratosphere. *Wea. Forecast.* **9**, 241–253.

Bacmeister, J. T., Schoeberl, M. R., Lait, L. R., Newman, P. A. and Gary, B. 1990. ER-2 mountain wave encounter over Antarctica: Evidence for blocking. *Geophys. Res. Lett* **17**, 241–253.

Baines, P. G. 1995. *Topographic Effects in Stratified Flow*. Cambridge University Press, Cambridge, 482 pp.

Barry, R. G. 2008. *Mountain Weather and Climate*. Cambridge University Press, Cambridge, 506 pp.

Baumgaertner, A. J. G. and McDonald, A. J. 2007. A gravity wave climatology for Antarctica compiled from Challenging Minisatellite Payload/Global Positioning System (CHAMP/GPS) radio occultations. *J. Geophys. Res.* **112**(D05103). doi:10.1029/2006JD007504.

Brasseur, O. 2001. Development and application of a physical approach to estimating wind gusts. *Mon. Wea. Rev.* **129**(1), 5–25.

Briggs, B. H. 1984. The analysis of spaced sensor records by correlation techniques, *Handbook for MAP*, Vol. 13, SCOSTEP Secr. Univ. of Ill., Urbana, pp. 166–186.

Dudhia, J. 1989. Numerical study of convection observed during the winter monsoon experiment using a mesoscale two-dimensional model. *J. Atmos. Sci.* **46**, 3077–3107.

Egger, J., Wamser, C. and Kottmeier, C. 1993. Internal atmospheric gravity waves near the coast of Antarctica. *Bound.-Layer Meteor.* **66**, 1–17.

Fritts, D. C. and Alexander, M. J. 2003. Gravity wave dynamics and effects in the middle atmosphere. *Rev. Geophys.* **41**(1), 1003. doi:10.1029/2001RG000106.

Haynes, P. 2005. Stratospheric dynamics. *Annu. Rev. Fluid Mech.* **37**, 263–293.

Holdsworth, D. A. and Reid, I. M. 2004. Comparisons of full correlation analysis (FCA) and imaging Doppler interferometry (IDI) winds using the Buckland Park MF radar. *Ann. Geophys.* **22**, 3829–3842.

Holdsworth, D. A., Vincent, R. A. and Reid, I. M. 2001. Mesospheric turbulent velocity estimation using the Buckland Park MF radar. *Ann. Geophys.* **19**, 1007–1017.

Holton, J. R. 1992. *An Introduction to Dynamic Meteorology*. 3rd Edition, Academic Press, London, 511 pp.

Hong, S.-Y., Noh, Y. and Dudhia, J. 2006. A new vertical diffusion package with an explicit treatment of entrainment processes. *Mon. Wea. Rev.* **134**, 2318–2341.

Höpfner, M., Larsen, N., Spang, R., Luo, B. P., Ma, J., and co-authors. 2006. MIPAS detects Antarctic stratospheric belt of NAT PSCs caused by mountain waves. *Atmos. Chem. Phys.* **6**, 1221–1230.

Jiang, Q. and Doyle, J. D. 2008. On the diurnal variation of mountain waves. *J. Atmos. Sci.* **65**, 1360–1377. doi:10.1175/2007JAS2460.1.

Jiang, Q., Smith, R. B. and Doyle, J. D. 2008. Impact of the atmospheric boundary layer on mountain waves. *J. Atmos. Sci.* **65**, 592–608. doi:10.1175/2007JAS2376.1.

Kärkäs, E. 2004. Meteorological conditions of the Basen nunatak in Western Dronning Maud Land, Antarctica, during the years 1989-2001. *Geophysica* **40**(1-2), 39–52.

Kikuchi, T. 1988. A case study of a wave-like cloud and gravity wave in the lower troposphere in Mizuho Plateau Antarctica. *Bound.-Layer Meteor.* **43**, 403–409.

King, J. C., Mobbs, S. D., Darby, M. S. and Rees, J. M. 1987. Observations of an internal gravity wave in the lower troposhere at Halley, Antarctica. *Bound.-Layer Meteor.* **39**, 1–13.

King, J. C. and Turner, J. 1997. *Antarctic Meteorology and Climatology*. Cambridge Univ. Press, New York, 409pp.

Kirkwood, S., Nilsson, H., Morris, R. J., Klekociuk, A. R., Holdsworth, D. A., and co-authors. 2008. A new height for the summer mesopause—Antarctica, December 2007. *Geophys. Res. Lett.* **35**(L23810). doi:10.1029/2008GL035915.

Kirkwood, S., Wolf, I., Dalin, P., Nilsson, H., Mikhailova, D., and co-authors. 2007. Polar mesosphere summer echoes at Wasa, Antarctica (73° s)—first observations and comparison with 68° n. *Geophys. Res. Lett.* **34**(L15803). doi:10.1029/2007GL030516.

Launiainen, J., Uotila, J., Vihma, T., Taalas, P., Karlsson, K., and co-authors. 1995. Meteorological observations at the Aboa station. *Antarctic Rep. Finland* **5**, 30.

Liu, H., Jezek, K., Li, B. and Zhao, Z. 2001. Radarsat antarctic mapping project digital elevation model version 2. Digital media.

Mercer, A., Richman, M., Bluestein, H. and Brown, J. 2008. Statistical modeling of downslope windstorms in Boulder, Colorado. *Wea. Forecast.* **23**, 1176–1194. doi:10.1175/2008WAF2007067.1.

Mlawer, E. J., Taubman, S. J., Brown, P. D., Iacono, M. J. and Clough, S. A. 1997. Radiative transfer for inhomogeneous atmosphere: RRTM, a validated correlated-k model for the long- wave. *J. Geophys. Res.* **102**(D14), 16663–16682.

Nappo, C. J. 2002. *An Introduction to Atmospheric Gravity Waves*. Academic Press, San Diego, 276 pp.

Noh, Y., Cheon, W., Hong, S.-Y. and Raasch, S. 2003. Improvement of the K-profile model for the planetary boundary layer based on large eddy simulation data. *Bound.-Layer Meteor.* **107**, 401–427.

Olafsson, H. and Bougeault, P. 1997. The effect of rotation and surface friction on orographic drag. *J. Atmos. Sci.* **54**, 193–210.

Peng, S. and Thompson, W. T. 2003. Some aspects of the effect of surface friction on flows over mountains. *Quart. J. Roy. Meteor. Soc.* **129**, 2527–2557.

Plougonven, R., Hertzog, A. and Teitelbaum, H. 2008. Observation and simulations of a large-amplitude mountain wave breaking over the Antarctic Peninsula. *J. Geophys. Res.* **113**(D16113). doi:10.1029/2007JD009739.

Preusse, P., Eckermann, S. and Ern, M. 2008. Transparency of the atmosphere to short horizontal wavelength gravity waves. *J. Geophys. Res.* **113**(D24104). doi:0.1029/2007/JD009682.

Rees, J. M., Denholm-Price, J. C. W., King, J. C. and Anderson, P. S. 2000. A climatological study of internal gravity waves in the atmospheric boundary layer overlying the Brund Ice Shelf, Antarctica. *J. Atmos. Sci.* **57**, 511–526.

Richard, E., Mascart, P. and Nickerson, E. C. 1989. The role of surface friction in downslope windstorms. *J. Appl. Meteor.* **28**, 241–251.

Scorer, R. S. 1949. Theory of waves in the lee of mountains. *Quart. J. Roy. Meteorol. Soc.* **74**, 41–56.

Skamarock, W. C., Klemp, J. B., Dudhia, J., Gill, D. O., Barker, D. M., and co-authors. 2007. A description of the advanced research wrf version 2. *NCAR/TN-468+STR NCAR TECHNICAL NOTE*. June 2005, Last revision: January 2007.

Smith, R. 1985. On severe downslope winds. *J. Atmos. Sci.* **42**, 2597–2603.

Thompson, G., Rasmussen, R. M. and Manning, K. 2004. Explicit forecasts of winter precipitation using an improved bulk microphysics scheme. Part I: description and sensitivity analysis. *Mon. Wea. Rev.* **132**, 519–542.

Tietäväinen, H. and Vihma, T. 2008. Atmospheric moisture budget over antarctica and southern ocean on the basis of era-40 reanalysis. *Int. J. Climatol* **28**, 1977–1995. doi:10.1002/joc.1684.

Virkkula, A., Asmi, E., Teinilä, K., Frey, A., Aurela, M., and co-authors. 2009. Review of aerosol research in Aboa and the surroundings. *Geophysica* **45**(1-2), 163–181.

Wacker, U., Ries, H. and Schttler, U. 2009. Precipitation simulation for Dronning Maud Land using the COSMO Model. *Antarctic Sci.* **21**, 643–662.

Watanabe, S., Sato, K. and Takahashi, M. 2006. A general circulation model study of the orographic gravity waves over Antarctica excited by katabatic winds. *J. Geophys. Res.* **111**(D18104). doi:10.1029/2005JD006851.

Whiteway, J. A. and Duck, T. J. 1996. Evidence for critical level filtering of atmospheric gravity waves. *Geophys. Res. Lett.* **23**(2), 145–148.

Yoshiki, M. and Sato, K. 2000. A statistical study of gravity waves in the polar regions based on operational radiosonde data. *J. Geophys. Res.* **105**(D14), 17995–18011.

Zilitinkevich, S. S. and Esau, I. 2005. Resistance and heat transfer laws for stable and neutral planetary boundary layers: Old theory, advanced and re-evaluated. *Quart. J. Roy. Meteorol. Soc.* **131**, 1863–1892. doi:10.1256/qj.04.143.